AAS 17-055

NARROWBAND REJECTION OF REACTION WHEEL AND ENVIRONMENTAL DISTURBANCES FOR THE WFIRST OMC TESTBED*

Joel Shields†, Fang Shi‡, Ray Lam‡, Tuan Truong‡, Keith Patterson‡

The Wide Field Infrared Survey Telescope (WFIRST) is a NASA observatory with two scientific instruments. The first is the Wide Field Instrument (WFI) designed to perform wide field imaging and surveys of the near infrared (NIR) sky. The second is a coronagraph (CGI) that will enable astronomers to detect and measure properties of planets in other solar systems. The coronagraph requires 0.5 milli-arcsecond (mas) RMS pointing per axis of the line of sight (LOS) to achieve a contrast of $1x10^{-9}$. This paper discusses the approach used for achieving this level of pointing performance on the occulting mask coronagraph (OMC) testbed at JPL. This testbed uses a low-order wavefront sensing (LOWFS) camera and fast steering mirror (FSM) to suppress injected LOS jitter and environmental LOS jitter. The injected jitter includes representative broadband spacecraft attitude control system (ACS) LOS motion and tonal LOS jitter caused by the reaction wheel assemblies (RWA). The environmental jitter includes thermal LOS variations and harmonics of the line noise. The LOWFS camera uses high flux from the obscured science target to achieve high rate measurements of the LOS. These measurements are augmented with fictitious RWA tachometer information and an estimate of the line noise frequency. A LOS servo using a combination of feedback and feedforward control is used in the testbed to compensate for all of the disturbance sources and to mitigate jitter caused by in-band camera noise. The feedforward uses a novel robust least mean squares (RLMS) filter algorithm to reject the RWA and line frequency tones. High fidelity models of the sensors, disturbances and actuator are presented in this paper. These models were developed as part of a simulation of the LOS control system. Performance results from the hardware testbed at the Jet Propulsion Laboratory (JPL) are discussed in this paper.

INTRODUCTION

The Wide Field InfraRed Survey Telescope (WFIRST), is a NASA observatory designed to settle essential questions in the areas of dark energy, exoplanets, and infrared astrophysics. The telescope has a primary mirror that is 2.4 meters in diameter with a compression ratio of 55. WFIRST will have two instruments, the Wide Field Instrument (WFI) developed at Goddard, and the Coronagraph Instrument (CGI) developed at JPL. The Coronagraph Instrument will perform

* © 2017 California Institute of Technology. Government sponsorship acknowledged.
† Corresponding Author, Senior Engineer, Guidance Navigation and Control Section, Jet Propulsion Laboratory, California Institute of Technology, 4800 Oak Grove Drive, Pasadena, CA 91109-8099. MS 198-326. Joel.F.Shields@jpl.nasa.gov
‡ Jet Propulsion Laboratory, California Institute of Technology

high contrast imaging and spectroscopy of dozens of individual nearby exoplanets. Coronagraphy on WFIRST will be a major step towards the long-term goal of a mission that can image habitable Earth-mass planets around nearby stars and measure their spectra for signs of life. Coronagraphs operate by blocking the light of the target star so that the dim light of the orbiting exoplanet is observable. A key performance metric for these instruments is the contrast which is a measure of the planet brightness relative to the star brightness. Contrast ratios on the order of 1e-9 are required for planet detection.

In order to advance the technology of coronagraph instruments a testbed is being developed at JPL that is a prototype of the flight instrument. This testbed is called the occulting mask coronagraph (OMC). It includes all the components of the flight instrument including a science camera, spectrometer, two deformable mirrors, fast steering mirror (FSM), and a wavefront sensing camera called the low-order wavefront sensing camera (LOWFS). The LOWFS is able to measure 10 components of the wavefront expressed in terms of Zernike coefficients, $Z_2 - Z_{11}$, at a rate of 500 to 1000 Hz depending on the type of camera used.[1] In this paper we are concerned with only the tip and tilt wavefront errors, Z_2 and Z_3. The contrast achievable by the coronagraph is highly sensitive to tip/tilt jitter and must be attenuated to less than 0.5 mas RMS per axis on the sky (OTS).

To mimic the wavefront errors that the CGI instrument will be subject to in flight, the testbed uses a jitter mirror (JM) to inject Z_2 and Z_3 distortions and an optical telescope assembly (OTA) to inject higher order wavefront errors. The OTA is a miniaturized primary and secondary mirror assembly which is actuated with a number of PZTs. For the jitter mirror a signal generator was developed that injects spacecraft attitude control system (ACS) line of sight (LOS) errors and tonal LOS errors due to the imbalances in the reaction wheel assemblies (RWA). In addition, disturbances from the lab environment also impact the performance of the coronagraph. These disturbances include thermal variations and an acoustic disturbance at harmonics of the line frequency which both impact the achievable contrast level. The disturbances are discussed next followed by a discussion on the design of the LOS control system. The latest testbed results for the LOS control system are then given which show the successful mitigation of all disturbance sources using a combination of low bandwidth feedback and a robust least mean squares (LMS) algorithm for feedforward tonal rejection.

DISTURBANCES

The integrated modeling team at Goddard has delivered to JPL estimates of the spacecraft buss motion due to in band ACS sensor noise and high frequency LOS structural jitter generated by the reaction wheels. These deliveries are continually evolving and in the testbed we have been using the "Cycle 5" delivery which is a relatively low fidelity model. Cycle 5 data assumes that there are 4 reaction wheels and reports only the jitter from the worst wheel at each wheel speed. The number of modes used in this delivery is also limited. Nonetheless, the amplitudes of the RWA jitter are similar to later deliveries of the integrated model.

We have made the assumption that the RWA disturbances are coherent but there is some concern that this may not be the case. The RWA disturbance tones are caused by static and dynamic imbalances as well as bearing imperfections. As the exported force and torque from the wheel is transmitted through the structure to the optical components these tones can change their frequency due to build-up of momentum caused by solar pressure. In addition, at higher frequency, noise in the tachometer servo will cause some level of wheel speed jitter. These frequency variations could cause large amplitude and phase variations of the optical LOS as the wheel tones transit through structural modes. Fast amplitude and phase variations could result in the LMS filter having trouble with tracking these changes if the time constant of the LMS parameter estimation is slower then

these variations. If this is indeed the case, then it has been proposed to use accelerometers placed throughout the structure to directly measure the LOS. The LMS approach discussed in this paper could easily be augmented with a tapped delay line to incorporate the accelerometer measurements. In fact, this approach is used in disk file servos to attenuate speaker noise in laptop computers as well as other applications.[2]

Spacecraft ACS

According to the Goddard team designing the ACS for WFIRST, the drift of the spacecraft LOS can be approximated by a second order shaping filter driven by Gaussian white noise with unit variance. For each axis of the spacecraft a simple model of the form,

$$\boldsymbol{\theta}_{\boldsymbol{LOS}}^{\boldsymbol{ACS}}(\boldsymbol{t}) = \frac{\boldsymbol{k\omega_n^2}}{\boldsymbol{s^2+2\zeta\omega s+\omega_n^2}}\boldsymbol{v}(\boldsymbol{t}), \tag{1}$$

is sufficient to characterize the motion of the spacecraft LOS. The RMS can be adjusted with k and the corner frequency is ω_n. The Goddard team is still designing the spacecraft ACS but the corner frequency can be expected to be in the 0.05 Hz to 0.2 Hz range. The current performance of the ACS is stated to be 4 mas with the requirement being 14 mas. This is extremely good stability given the ACS sensor suite that is baselined for the mission but these GN&C sensors are aided by narrow field measurements from the WFI focal plane. This model was discretized and included in the jitter mirror disturbance signal generator. The user interface for the testbed includes an option for adjusting the RMS of this signal.

Reaction Wheel Assemblies

The Cycle 5 reaction wheel model used by the integrated modeling team is based on a vendor supplied 73 harmonic model for the Honeywell HR14-75. The momentum capacity for these wheels is 75 N-m-s and the spec. imbalances are 0.48 gram-cm and 13.7 gram-cm^2 for the static imbalance and dynamic imbalance, respectively. The exported force and torque from this model was applied to the structural model and optical metrics for the wavefront jitter were generated. For the LOS wavefront, a model of the following form is used to calculate the per axis tonal jitter from this disturbance source,

$$\boldsymbol{\theta}_{\boldsymbol{LOS}}^{\boldsymbol{RWA}}(\boldsymbol{t}) = \sum_{\boldsymbol{i=1}}^{\boldsymbol{N_h}} \boldsymbol{f_i}\big(\boldsymbol{\Omega}(\boldsymbol{t})\big)\boldsymbol{sin}(\boldsymbol{2\pi h_i \Omega}(\boldsymbol{t})\boldsymbol{t} + \boldsymbol{\phi_i}), \tag{2}$$

where $\Omega(t)$ is the wheel speed in Hertz and f_i, h_i, and ϕ_i are the harmonic amplitudes, harmonic coefficients and harmonic phases, respectively. N_h is the number of harmonics, 73. Most of the energy in this disturbance is in the fundamental and a subharmonic. The rest of the overtones contribute a relatively small amount of energy to the total RMS. For wheel speeds up to 1200 RPM this puts most of the energy below the structural resonances which start at ~20 Hz. As a function of wheel speed the total RMS for this disturbance is well above 0.5 mas which requires that it be attenuated by a factor of 30-40 dB. At 600 RPM, for example, the RMS of the RWA disturbance is above 6 mas RMS due to isolator amplification in this region. This disturbance signal is added to the ACS and options were created in the testbed user interface to scale its amplitude.

Line Noise

A common problem in ground based testbeds is that they are subject to line noise from the wall power. Noise at 60 Hz and higher harmonics often contaminates sensors and DAC commands. It is often hard to tell if this noise is actually causing real motion or just effecting the sensors. In this case, exhaustive investigations were performed to determine if it was real motion since the contrast performance of the testbed was significantly degraded at 120 Hz. If the motion was not real, then trying to compensate for it would make the jitter worse.

The evidence gathered was conclusive in determining that the 120 Hz signal was real. The first piece of evidence was that a 120 Hz signal was observed in both the science camera and LOWFS camera as well as in bench mounted accelerometers. It is significant that is was observed in the cameras since they are typically immune to this sort of noise. The line noise disturbance was also highly correlated with the building temperature and subsequently with the air handling activity which was consistent with the hypothesis that the HVAC system was causing a percussive force on the vacuum chamber. This percussive force would not have to travel through the optical bench isolators since large cable bundles directly connect the side of the vacuum chamber to the optical bench. The cameras only measured the 120 Hz disturbance in the vertical channel which is consistent with the fact that the bench mounted accelerometers only measured the 120 Hz in the direction normal to the table.

Given the assumption that the 120 Hz LOS measurements represented real motion an effort was launched to redesign the controller to attenuate it. The challenge was not just the amplitude of the 120 Hz signal but that it also varied in frequency. Spectrum measurements from the accelerometers revealed that the frequency varied by +/-0.1 Hz over the course of 18 hours. Adding an LMS ringer at 120 Hz was not, by itself, sufficient to consistently cancel this disturbance. The disturbance frequency would drift away from the ringer location, or through it in a matter of a few minutes. A more robust method of cancelling this disturbance was necessary. This led to the development of a novel LMS filter that uses multiple ringers placed next to each other that produced a broader band "flat-top" ringer. We have taken to calling this the Robust LMS filter (RLMS). The design of this filter and its performance is discussed in following sections of this paper.

Camera Noise

The coronagraph operates by blocking the star light with a mask in the pupil image. This blocked light is diverted to the LOWFS camera which uses the relatively high photon flux (high relative to the planet light) to estimate the wavefront errors. It is important to keep in mind that the target star brightness can vary based on its stellar magnitude and that for bright stars the photon flux will result in relatively low noise measurements of the wavefront LOS whereas dim stars will have higher noise measurements. This effects the achievable bandwidth of the feedback servo as high noise LOS measurements will result in excessive in band jitter. Given the 500 Hz sample rate in the OMC testbed, delays in the servo loop would only limit the bandwidth to approximately 30 Hz. Closing a feedback loop at this bandwidth with the star brightness used in the testbed, resulted in too much jitter. The closed loop bandwidth had to be reduced to 4 Hz because of the noise in the LOS measurements. This low bandwidth, however, does effect the ability to attenuate the ACS disturbance. An optimization procedure for balancing the errors from camera noise and ACS disturbances is discussed below in the section on the feedback design.

Open loop measurements of the LOWFS LOS sampled at 500 Hz were used to characterize the camera noise. The PSD of these measurements contained thermal and environmental jitter but the floor of these PSDs were used to estimate the RMS of the Z_2 and Z_3 measurements caused by shot noise. When the testbed was configured with the shaped pupil mask (SPC) the noise floor was 4.6 nm for the Z_2 measurement and 4.4 nm for the Z_3 measurement. On the sky, this is equivalent to approximately 20 mas, well above our pointing requirement of 0.5 mas.

ACTUATOR MODELING AND CHARACTERIZATION

The FSM used in the OMC testbed was inherited from the Space Interferometer Mission (SIM) project. This FSM was a momentum compensated design with three PZTs located on the corners of an equilateral triangle. Each PZT is mounted in a parallelogram flexure that moves both the mirror and a reaction mass. The flexure also serves to amplify the motion by a factor of 2 resulting

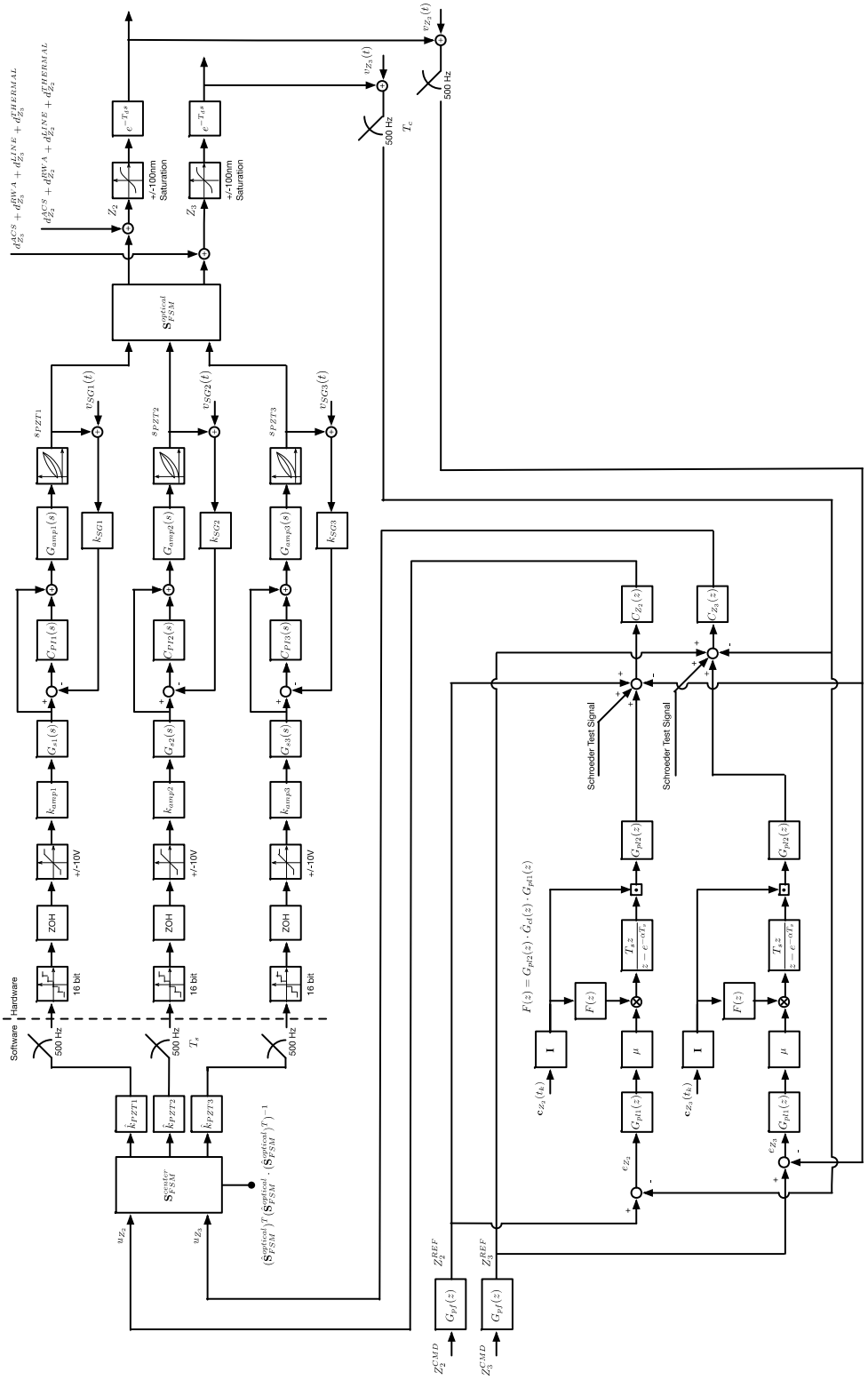

Figure 1. LOS control system for OMC testbed. The plant consists of the three FSM PZTs, optical sensitivity and LOWFS camera. Disturbances and feedback and LMS feedforward loops are also depicted.

in a stroke of +/-72 arc seconds in mechanical space. Dynamometer measurements of the exported force and torque with and without the reaction mass indicated that the momentum compensation was less then successful. The mirror side modes did not match the modes of the reaction mass though tuning of the stiffness and mass properties may remedy this.

One interesting aspect of the SIM FSM is that the pivot point of the mechanism was designed to be on the surface of the mirror. This was important for SIM since it decoupled the pathlength and pointing control loops and may have utility for the WFIRST project in terms of mitigating beamwalk.

Strain gauges mounted directly on the PZTs provided local feedback for linearizing the hysteresis[3] of the PZTs. The bandwidth of this local loop was set to 150 Hz. This bandwidth was limited by the first mode of the mechanism at 900Hz. The local loop was implemented in the electronics as an analog PI compensator. The analog electronics also had a prefilter for smoothing DAC noise and allowed for attenuating the DAC voltage. Both the prefilter and gain attenuation were used to minimize jitter from DAC noise and quantization. The PZT amplifier selected for the testbed was a custom JPL design with chopping which eliminated the effect of line noise in the strain gauge sensor.

To meet the 0.5 mas stability requirement the actuator used to suppress the jitter must itself be stable to a fraction of the total stability requirement. To assess the FSM stability, laser metrology was used to monitor the motion of a single PZT. This testing was done in vacuum to avoid atmospheric distortions of the laser and with the FSM mounted on an isolated optical bench to avoid mechanical vibrations. Tests to establish the background jitter and laser metrology resolution were performed as well as tests to determine the jitter from process or amplifier noise and strain gauge noise. Based on the background tests, the noise floor for these tests was determined to be 0.3 nm RMS of PZT displacement or 1.0 mas in mechanical angle space. The 0.5 mas stability requirement in mechanical angles at the FSM is 13.75 mas which is 13.75 times the sensing resolution.

Turning on and off the PZT amplifier demonstrated no appreciable increase in jitter relative to the background cases indicating that amplifier noise was not a significant source of jitter. Tests with the strain gauge loop closed indicated jitter of 2.4 mas RMS, 2.4 times the background jitter, but still a small portion of the stability requirement of 13.75 mas. Since there are three PZTs turned on during operation, we can expect this jitter to increase by a factor of $\sqrt{3}$ assuming the jitter of three PZTs is independent. This puts the FSM stability at 4.15 mas or less then 1/3 of the overall stability requirement.

Transfer function measurements from the strain gauge sensor noise to PZT output displacement allowed one to solve for the PI compensator gains of the strain gauge loop. A full model of the PZT with amplifier servo electronics is shown in Figure 2. Note the block diagram in this Figure indicates a feedforward path that increases the agility of the servo and a smoother for limiting the bandwidth of input noise. In addition, the DAC voltage is attenuated by a factor of 1/100. This was done to mitigate the effect of DAC noise. Assuming a DAC error of 3 bits, this maps to 0.03 nm of PZT motion or 0.1 mas in angle space, a negligible amount of 13.75 mas. The drawback of this attenuation is that the stroke of the FSM is severely compromised to under an arc second. The flight design would have to have second stage mechanism or a second coarse DAC summed with the high resolution DAC.

OPTICAL SENSITIVITY

To determine the mapping from the PZT displacements to LOWFS camera measurements each PZT was modulated with a square wave voltage and the resulting camera measurements were recorded. From this data, the 2x3 optical sensitivity matrices from the FSM and JM PZTs to the camera measurements were derived. Due to the actuation geometry and clocking between the steering mirrors and camera frame these sensitivity matrices are coupled in the sense that moving any one of the PZTs can change both camera measurements.

FSM Steering

In order to decouple the optical sensitivities, the control software uses a pseudoinverse of the form,

$$\boldsymbol{M_{FSM}} = \boldsymbol{S_{FSM}^T}(\boldsymbol{S_{FSM}}\boldsymbol{S_{FSM}^T})^{-1}, \tag{3}$$

where $\boldsymbol{S_{FSM}}$ is the optical sensitivity matrix for the FSM. A similar steering matrix can be generated for the JM. At low frequency, multipling the steering matrix by the optical sensitivity results in an identity relationship between the tip tilt commands, Z_2^{CMD} and Z_3^{CMD} and the tip tilt measurements, $Z_{2m}$and Z_{3m}. At frequencies above 150 Hz the decoupling is less effective because of the limited bandwidth of the PZT servo electronics.

To take advantage of the full workspace of the FSM an additional step in the steering is necessary. Because of the triangular arrangement of the three PZTs the available tip tilt angles of the FSM forms a hexagon when they are plotted versus each other. Moving the PZTs without a net piston does not recover the full hexagonal workspace. To take advantage of this extra workspace the following optimization must be performed,

$$\mathbf{min}(\mathbf{max}([\boldsymbol{s_{PZT1}}\ \boldsymbol{s_{PZT2}}\ \boldsymbol{s_{PZT3}}])), \tag{4}$$

where the three PZT displacements are those obtained from using the steering matrix. The solution to this optimization problem is to simply piston all three PZTs by an amount equal to $-(s_{min} + s_{max})/2$, where s_{min} is the minimum PZT displacement and $s_{max}$is the maximum of the three PZT displacements.

FEEDBACK CONTROL DESIGN

The feedback control design is used to address jitter from thermal sources, jitter from the injected ACS and jitter from in band sensor noise. Jitter from the injected RWA signal and lab line noise is addressed with the feedforward loop. This architecture allows one to independently use the feedback to attenuate broadband sources of jitter and the feedforward to attenuate tonal sources of jitter. The structure of the feedback compensator was a simple integrator with a pole at high frequency for steeper roll off of the gain. The integral gain of the feedback design is a compromise in bandwidth. One wants a high bandwidth to attenuate the ACS disturbance but a low bandwidth to avoid unnecessary jitter from sensor noise.

To find the optimal bandwidth, the RSS of the RMS of the sensor jitter and RMS of the ACS jitter can be computed as a function of the integrator gain or equivalently the closed loop bandwidth. The RMS sensor jitter is calculated by integrating the spectrum of the complementary transfer function driven by a continuous time equivalent of the camera noise characterized from the open loop camera data. Similarly, the RMS jitter from the injected ACS is calculated by integrating the spectrum of the sensitivity transfer function times the ACS shaping filter, Equation (1). The integral gain that minimizes the RSS is then selected as the optimal gain for the feedback compensator. The optimal gain will in general have different RMSes for the two jitter contributions.

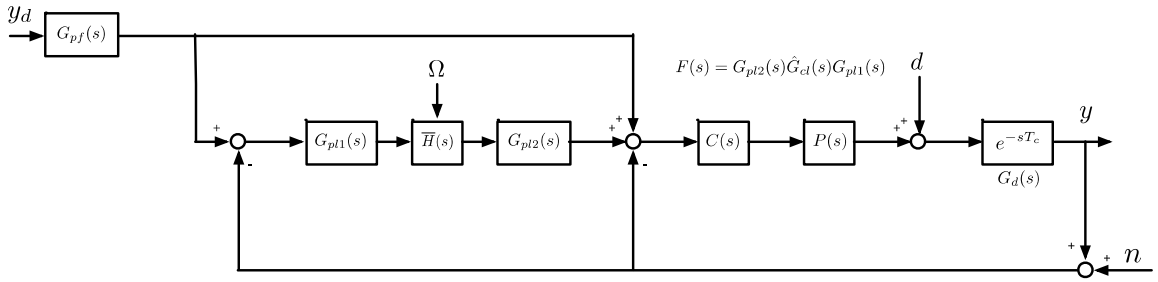

Figure 2. Simplified continuous time representation of the robust LMS filter. The LMS filter is seeded with tachometer measurements and line frequency estimates.

LMS CONTROL DESIGN

The LMS design is inspired from the linear time invariant (LTI) properties of modulation and demodulation. When a harmonic sin/cos regressor is used as the basis functions for the LMS filter, at steady state, the filter can be represented as a linear transfer function,

$$\widehat{\boldsymbol{d}} = \overline{\boldsymbol{H}}(\boldsymbol{s})\boldsymbol{e} \qquad \overline{\boldsymbol{H}}(\boldsymbol{s}) = \boldsymbol{\mu}\sum_{\boldsymbol{i=1}}^{\boldsymbol{m}} \boldsymbol{H_i}(\boldsymbol{s}), \tag{5}$$

where $\hat{d}$ is the estimate of the disturbance to be canceled and e is the servo error of the feedback loop. [4] The variable μ is the gain of the LMS filter and m is the number of disturbance tones to be cancelled, in this case 3. $H_i(s)$ is given by,

$$\boldsymbol{H_i}(\boldsymbol{s}) = \frac{\boldsymbol{F_{Re}(\omega_i)}}{\boldsymbol{2}}(\boldsymbol{\Gamma(s - j\omega_i) + \Gamma(s + j\omega_i)}) + \frac{\boldsymbol{F_{Im}(\omega_i)}}{\boldsymbol{2}}(\boldsymbol{\Gamma(s - j\omega_i) + \Gamma(s + j\omega_i)}), \tag{6}$$

where $\Gamma(s) = 1/(s + \alpha)$ is the gradient algorithm with leakage and $F(s)$ is the so called secondary path transfer function, [5] in this case the loop gain from the output of the LMS filter through the feedback transfer function and back to the input of the LMS filter. $F(s)$ is indicated in Figures 1 and 2. The advantage of this representation is that we can now use all the conventional LTI tools to design and analyze the control system. Each $H_i(s)$ is a second order ringer with a resonance at ω_i, finite DC gain and first order roll off at high frequency.

Figure 1 shows the full architecture of the LOS control system with the plant, disturbance sources, feedback and feedforward control. A simplified, SISO continuous time version, of Figure 1 is shown in Figure 2. Recall that the feedback loop has a limited bandwidth so that driving a signal through the input to this servo to attenuate higher frequency disturbances will require some amplification before being applied. This is the purpose of $G_{pl2}(s)$ shown in Figures 1 and 2. We use the zero phase error tracking controller (ZPETC) to invert the closed loop transfer function of the feedback servo. [6] This inversion should try to extend the unity gain out to as high a frequency as possible so that high frequency disturbances can be attenuated without suffering from gain loss. We can represent the closed loop feedback transfer function as,

$$\boldsymbol{G_{fb}}(\boldsymbol{s}) = \frac{\boldsymbol{kB^s(s)B^u(s)}}{\boldsymbol{A(s)}}, \tag{7}$$

where we have partioned the zeros into stable and unstable polynomials. In this case, non-minimum phase zeros occur due to using a second order Pade approximation for the camera delay. The ZPETC has the form,

$$\boldsymbol{G_{ZPETC}}(\boldsymbol{s}) = \frac{\boldsymbol{A(s)B^u(-s)}}{\boldsymbol{kB^s(s)B^u(0)B^u(0)}}. \tag{8}$$

Multiplying Equation (7) by Equation (8) leaves, $B^u(-s)B^u(s)/B^u(0)B^u(0)$, which has zero phase distortion and unity gain at low frequency. Unfortunately, Equation (8) by itself is not proper so we must add some poles to make it a causal and implementable transfer function. In this case we need to add 8 poles since $A(s)$ has 7 poles, $B^u(s)$ has order 2 and $B^s(s)$ has order 1. We choose to use a Butterworth filter with a corner frequency of 180 Hz since it is a pole only filter and has a sharp stopband. Note that adding the Butterworth poles to $G_{pl2}(s)$ ends up distorting the phase but the gain remains unity out to the corner frequency of the Butterworth poles. The phase distortion can be accounted for in the secondary path transfer function used in the LMS filter. What is important at this point is that the gain is not attenuated.

Robust Ringers

A common problem with LMS filters is that if the disturbance frequency information is not precise the attenuation achieved can be significantly degraded. In this case, we have empirical evidence that the line frequency disturbance does drift and that a single LMS ringer was not sufficient to attenuate this disturbance with reasonable confidence. Placing multiple ringers in close frequency proximity can provide a broader band gain and be more robust to disturbances frequencies that drift. In this application, for each disturbance tone that we want to attenuate, 7 LMS ringers were placed next to each other with a frequency separation of 0.04 Hz leading to a "flat-top" ringer with a width of 0.24 Hz. More ringers could be added if desired to create a wider flat-top. The leakage parameter, α, was used to blend the gain of the ringers which made the peak of the robust ringer uniform. Adding 7 ringers for each disturbance tone greatly increases the dimension of the harmonic regressor used by the LMS filter. Since each regressor signal has to be filtered by the secondary path transfer function, $F(s)$, computation can quickly become an issue since the order of $F(s)$ is 24 in this application. To overcome this issue, the gain and phase of F(s) as a function of frequency was implemented as a lookup table which required far less computation. For example, a regressor basis function for frequency, ω_i, would be,

$$\begin{bmatrix} \boldsymbol{c_{Z_2}(t)} \\ \boldsymbol{c_{Z_3}(t)} \end{bmatrix} = \begin{bmatrix} \mathbf{cos}(\boldsymbol{2\pi\omega_i t}) \\ \mathbf{sin}(\boldsymbol{2\pi\omega_i t}) \end{bmatrix}. \tag{9}$$

After filtering through $F(s)$, this basis becomes,

$$\begin{bmatrix} \boldsymbol{c^f_{Z_2}(t)} \\ \boldsymbol{c^f_{Z_3}(t)} \end{bmatrix} = \begin{bmatrix} \mathbf{A}(\boldsymbol{\omega_i})\mathbf{cos}(\boldsymbol{2\pi\omega_i t + \phi(\omega_i)}) \\ \mathbf{A}(\boldsymbol{\omega_i})\mathbf{sin}(\boldsymbol{2\pi\omega_i t + \phi(\omega_i)}) \end{bmatrix}, \tag{10}$$

where $\mathrm{A}(\omega_i)$ and $\phi(\omega_i)$ are obtained from the lookup table.

Referring to Figure 2 we can write transfer functions that will provide some insight into how the control system operates. First note that the reference input y_d is used to add offsets to the instrument LOS and is added to the output before being sent to the LMS filter. This presents an AC coupled signal to the LMS and reduces the number of parameters that the LMS needs to estimate. Setting this input to zero, the transfer functions from the camera noise input and disturbance input to the LOS output can be written as,

$$y(s) = \frac{G_d(s)}{\left(1+G_d(s)C(s)P(s)\right)\left(1+\frac{G_d(s)C(s)P(s)}{1+G_d(s)C(s)P(s)}G_{LMS}(s)\right)}d(s) - \frac{G_d(s)C(s)P(s)\left(1+G_{LMS}(s)\right)}{\left(1+G_d(s)C(s)P(s)\right)\left(1+\frac{G_d(s)C(s)P(s)}{1+G_d(s)C(s)P(s)}G_{LMS}(s)\right)}n(s), \tag{11}$$

where $G_{LMS}(s)$ is given by,

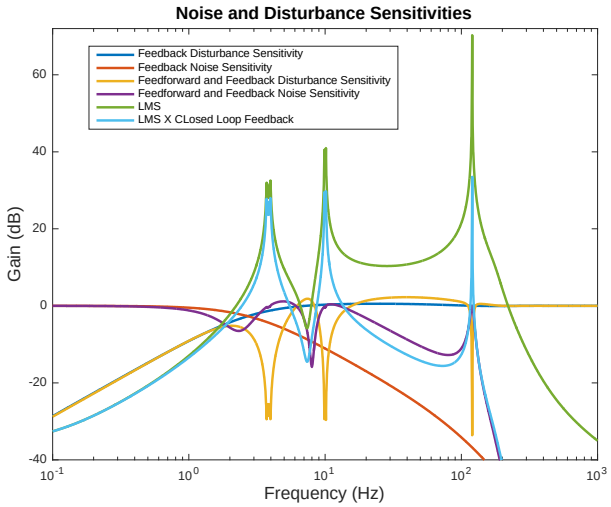

Figure 3. Bode magnitude plots for a wheel speed of 600 RPM showing the sensitivity and complimentary sensitivity transfer functions with and without the LMS feedforward. Also shown are the LMS open loop gain and LMS and feedback loop gain. Note the broadband gain of each ringer with robustifies the attenuation in the presence of regressor frequency error.

$$\boldsymbol{G_{LMS}(s) = G_{pl2}(s)\bar{H}(s)G_{pl1}(s).} \tag{12}$$

Note that when $G_{LMS}(s) = 0$ these equations revert to the traditional closed loop sensitivity and complimentary sensitivity. When $G_{LMS}(s) \neq 0$ the disturbance signal gets attenuated by the LMS at frequencies where the LMS gain is high, in addition to the feedback attenuation. Figure 3 shows the frequency response of these transfer functions with and without the LMS as well as the open loop gains. The first line shows the feedback disturbance sensitivity with large low frequency attenuation. Looking at the feedforward and feedback disturbance sensitivity the LMS adds attenuation at select frequencies without much distortion of the feedback disturbance sensitivity. The compensator $G_{pl1}(s)$ is used to lower the feedforward loop gain at low frequencies so that $G_{LMS}(s)$ is near zero and thus has little effect on the disturbance. $G_{pl1}(s)$ is a phase lead compensator of the form,

$$\boldsymbol{G_{pl1}(s) = \frac{(1/2\pi f_z)s+1}{(1/2\pi f_p)s+1}\frac{f_z}{f_p},} \tag{12}$$

with $f_z < f_p$. The DC gain of $G_{LMS}(s)$ can accumulate due to the fact that we are using so many ringers per disturbance tone. $G_{pl1}(s)$ compensates for this accumulation and the resultant changes to the sensitivity and complementary sensitivity transfer functions.

TESTBED DATA

Figure 3 demonstrates the Z_2 performance of the RLMS algorithm in the real time OMC testbed operating at 500 Hz. For this initial test of the LOS control system, the gain margin was set to a relatively conservative 14 dB. This resulted in approximately 30 dB of attenuation for each of the three tones being rejected. Future testing will reduce the gain margin and improve the tonal rejection. Three PSDs are plotted in Figure 3, the spectrum of the open loop disturbance with 4 mas RMS ACS jitter and 600 RPM RWA, the spectrum with only feedback operating and the spectrum with both feedback and feedforward. During this particular test the line disturbance happened to be at 119.7 just off the edge of the flat-top ringer centered at 120 Hz. At this frequency, the theoretical

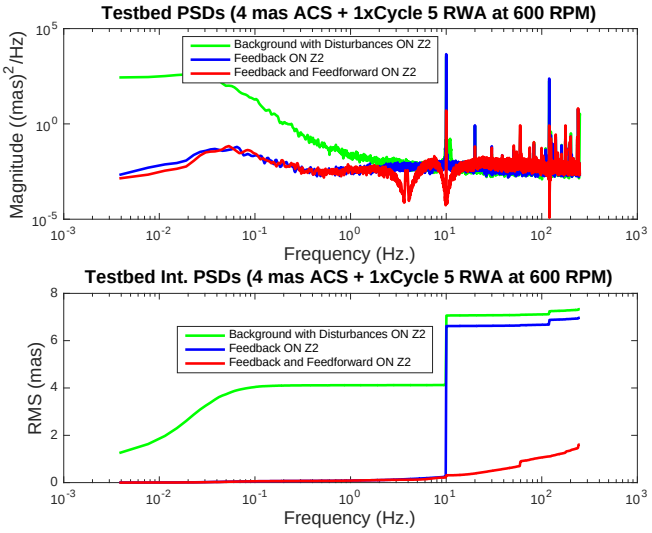

Figure 4. Open loop and closed loop testbed PSDs of the camera measurements demonstrating open loop jitter, feedback and feedforward attenuation.

attenuation was -21.8 dB. Looking at the PSDs in this region the difference between the open loop and closed loop with

feedforward responses demonstrated an attenuation by a factor of 17.1 slight better than the theoretical prediction. At 10 Hz the attenuation was 30 dB which is consistent with the theoretical prediction. For this wheel speed, the subharmonic had very little energy and as a result the ringer at this frequency had little effect on reducing the jitter. Note that the discontinuities in the integrated PSD (RMS) subplot at 10 Hz for the open loop and feedback only cases show roughly the same tonal RMS contribution in spite of the different sized steps. The RMS at the 10 Hz jump is given as,

$$\boldsymbol{\theta}_{\boldsymbol{RMS}}^{\boldsymbol{jump}} = \sqrt{\left(\boldsymbol{\theta}_{\boldsymbol{RMS}}^{\boldsymbol{f+}}\right)^{\mathbf{2}} - \left(\boldsymbol{\theta}_{\boldsymbol{RMS}}^{\boldsymbol{f-}}\right)^{\mathbf{2}}}, \tag{13}$$

where f^- and f^+ are the frequencies just before and after the jump. This equation evaluates to 5.7 mas for the open loop case and 6.6 mas for the feedback case. The slightly larger RMS of the jump can be explained by the slight amplification of disturbances in this region of the feedback sensitivity transfer function.

The total RMS with both the feedback and feedforward loops closed was 1.43 mas. This RMS includes sensor noise, however. Since the control loop has low pass characteristics not all of the sensor noise is actual jitter. PSDs of the simulated true jitter which omits much of the sensor noise reports jitter well below the 0.5 mas requirement.

CONCLUSION

In this paper we have described the LOS pointing system for the OMC testbed. The disturbances were modeled based on the expected flight performance of the spacecraft. These disturbances were injected into the LOS of the instrument using a JM. The testbed is also subjected to 120 Hz environmental line noise which had to be attenuated because of its adverse impact on contrast. The FSM actuator and its support electronics were extensively characterized with laser metrology and the actuator was found to be stable enough to support the overall LOS pointing requirement. Models

of the FSM were developed to support simulations and development of the real time control code used in the testbed.

The control system consists of a feedback loop optimally shaped to minimize jitter from ACS disturbances and in band camera noise and a feedforward loop that uses a RLMS filter to reject tonal disturbances. The RLMS uses multiple ringers to cancel each tone resulting in wider band rejection of tonal disturbances relative to conventional LMS filters. The RLMS filter is also aided by pre- and post- filters for canceling the roll off of the feedback loop and for compensating for low frequency distortion of the feedback sensitivity transfer function.

The RLMS filter was implemented in the OMC testbed and the experimental results are consistent with the theoretical predictions. We are currently looking at how to extend this control design to the flight system which may have non-coherent RWA disturbances. The RLMS filter can be augmented with accelerometer measurements of the instrument LOS if the time constant of the RLMS with tachometer/frequency information is not fast enough to track changes in the disturbance phase and gain. More recent deliveries from the integrated modeling team at Goddard suggest that the RWA disturbance may contain more disturbance energy at higher frequency.

ACKNOWLEDGMENTS

The work described in this paper was carried out at the Jet Propulsion Laboratory, California Institute of Technology, under contract with the National Aeronautics and Space Administration.

REFERENCES

[1] F. Shi and K. Balasubramanian and R. Hein and R. Lam and D. Moore and J. Moore and K. Patterson and I. Poberezhskiy and J. Shields and E. Sidick and H. Tang and T. Truong and J. K. Wallace and X. Wang and D. Wilson, "Low Order Wavefront Sensing and Control for WFIRST-AFTA Coronagraph." *JATIS* 2(1), 2016.

[2] S. Pannu and R. Horowitz, "Increase Disturbance Rejection for Hard Disk Drives Using Accelerometers." *Journal of Information Storage and Processing Systems*, Vol. 1, No. 1, pp. 95-103, Jan. 1999.

[3] J. Shields and S. Sirlin and M. Wette, "Starlight Pointing Subsystem for the Formation Interferometer Testbed (FIT)." Big Sky, Montana, March 2002 IEEE Aerospace Conference.

[4] D. Bayard, "A General Theory of Linear Time-Invariant Adaptive Feedforward Systems with Harmonic Regressors." *IEEE Transactions on Automatic Control*. Vol. 45, No. 11, Nov. 2000.

[5] B. Farhang-Boroujeny, Adaptive Filters Theory and Applications, Second Edition, Wiley, 2013.

[6] M. Tomizuka, "Zero Phase Error Tracking Controllers." *ASME Journal of Dynamic Systems, Measurement and Control*, Vol. 109, pp. 65-68, 1987.